Balancing degradation and tissue integration: a coupled-dynamics model of the mechanical performance of biodegradable hernia meshes

Abstract. Biodegradable meshes offer an alternative to permanent synthetic meshes that avoids their long-term complications, but their adoption remains limited by a substantial recurrence rate. The outcome of a repair is determined during a transition period in which the polymer is gradually resorbed and the mechanical load is progressively transferred to the integrating host tissue. The strength of the implant–tissue composite must be maintained throughout this period to resist tearing and recurrence, and its stiffness should approach that of the surrounding tissue to reduce foreign-body sensation. This evolution is difficult to predict because it emerges from many coupled factors spanning polymer chemistry, cell biology, and mesh architecture. We present a reduced-order model based on coupled ordinary differential equations that resolves these mechanisms into the time-dependent strength and stiffness of the composite. Calibrated to published Phasix (P4HB) data on molecular-weight retention and ball-burst strength, the model shows that strength passes through a minimum—the strength valley—during the transition and must remain above a rupture threshold, while stiffness declines from a polymer-dominated value through a transient minimum toward the tissue value; both conditions are satisfied only when degradation and tissue integration proceed at matched rates. The strength minimum is governed mainly by degradation chemistry and alleviated by a mid-range pore size. The model takes the Voigt (parallel, upper-bound) composite law as its nominal estimate and brackets it with a conservative lower bound; this bracket straddles the rupture floor, so the safety margin is conditional on the composite mixing rule. A global sensitivity analysis shows that both failure modes are governed by a few shared levers—degradation chemistry and tissue-secretion rates—while the many fine kinetic parameters hardest to identify individually (enzyme, gel-point, and maturation constants) are among the least influential. A robust-design analysis then shows the safe window to be co-determined by host tissue integration: under adverse tissue kinetics no mesh design alone remains safe, pointing to tissue-side factors as a complementary lever—and a possible explanation for recurrences not attributable to mesh failure. The framework converts the qualitative principle of matching degradation to tissue integration into quantitative, parameter-level guidance for the design of bioresorbable meshes.

Keywords: biodegradable hernia mesh; mechanical performance; strength and stiffness; coupled dynamics; tissue integration; robust design.

1 Introduction

Hernia is among the most common conditions treated by surgeons, and mesh-based tension-free repair is the standard of care (Brown, 2010; Bilsel and Abci, 2012; Pott et al., 2012). Permanent synthetic meshes provide reliable acute support, but as a retained foreign body they are linked to chronic pain, infection, seroma, shrinkage, and adhesion, and hernia recurrence remains non-negligible (Bellón et al., 2007; Deeken and Lake, 2017; Pott et al., 2012; Todros et al., 2015; Brown, 2010)—driving the search for materials that do not stay in the body indefinitely.

The two outcomes that matter most—discomfort and recurrence—have distinct mechanical origins. Foreign-body sensation and chronic pain arise from a mismatch between the mesh stiffness and that of the surrounding tissue: a mesh much stiffer than the abdominal wall is palpable and may erode (Deeken and Lake, 2017; Pott et al., 2012). Recurrence is a failure of strength: the construct tears or cannot sustain the peak load (Brown, 2010; Bilsel and Abci, 2012). A successful mesh must therefore control both its strength (to avoid rupture) and its stiffness (to stay unobtrusive) throughout its life.

Biodegradable meshes were developed to remove the permanent foreign body: the polymer resorbs and is replaced by integrating host tissue (P4HB/Phasix, Bio-A, PDO) (Deeken and Matthews, 2013; Martin and Williams, 2003; Heidari et al., 2024; Fatkhudinov et al., 2018). Their defining risk, however, is that the mechanical properties are no longer fixed: as the polymer degrades, strength and stiffness fall and the load must transfer to the integrating tissue across a transition period. If degradation outruns integration the construct may fail (recurrence); if too slow, the patient endures a stiff foreign body longer than needed. Success is decided by how strength and stiffness evolve through this transition—that is, by the balance between degradation and tissue integration long advocated in tissue engineering (Hutmacher, 2001; Drury and Mooney, 2003; Hollister, 2005; Pascual et al., 2012).

This evolution is hard to characterise. In-vivo studies are slow, costly, and too sparse in time to explore the design space (Deeken and Matthews, 2013; Fatkhudinov et al., 2018). Existing models cover only part of the problem: degradation models track the polymer in isolation, without the replacing tissue (Pan et al., 2022; Metters et al., 2000; Göpferich, 1996; Ford Versypt et al., 2013), while tissue-growth models do not resolve the load-bearing trajectory of a finished mesh (Akalp et al., 2016; Dhote et al., 2013; Prendergast et al., 1997; Checa and Prendergast, 2009). None couple both into the time-dependent strength and stiffness of an implant–tissue composite, calibrated to a real mesh, and turn it into a design tool.

This raises a predictive question: *how will the strength and stiffness of a given biodegradable mesh decay as it resorbs, and can that trajectory be predicted accurately enough to design meshes whose composite strength never falls below the tissue's load-bearing threshold?*

Here we present such a model—a reduced-order coupled ODE system linking polymer physics (network integrity, swelling, hydrolytic and enzymatic degradation), cell biology (fibroblast proliferation, collagen deposition, MMP/LOX remodelling), and mesh architecture into the time-dependent

strength and stiffness of the composite. Strength is the primary metric (recurrence is tearing); stiffness is tracked for comfort. The model is calibrated to Phasix (P4HB) molecular-weight-retention and ball-burst data.

We show that strength passes through a "strength valley"—a transient minimum during the hand-off—that is governed mainly by degradation chemistry, alleviated by a mid-range pore size, and cleared only when degradation and integration rates match. (The stiffness margin traces a deeper, later valley of its own, but because recurrence is a tearing rather than a softening failure, the strength valley is the binding constraint.) We define a safe-design window under the nominal (upper-bound) composite law and test it against a conservative lower bound, and a robust-design map that stays safe under biological uncertainty, since global sensitivity shows the parameters hardest to identify are also the least influential. The framework turns the qualitative degradation–integration balance into quantitative, parameter-resolved design guidance.

2 Model

2.1 Overview and state variables

The mechanical state of the repair is set by two coupled processes—polymer degradation and tissue integration—acting on a shared mesh architecture. We follow six state variables over time t (in weeks), each normalised to the interval $[0, 1]$: the remaining polymer mass m and network integrity ρ_x; the fibroblast density c, deposited collagen (extracellular matrix) e, matrix-metalloproteinase (MMP) concentration z, and collagen maturity ℓ (crosslinking by lysyl oxidase). These feed two modules—a material-degradation block and a tissue-integration block—whose outputs combine in a composite-mechanics block into the time-dependent strength and stiffness of the implant–tissue composite (Fig. 1); the parameters are summarised in Table 1.

For a chemically crosslinked network, ρ_x is the crosslink density; for a linear semicrystalline thermoplastic such as P4HB, it serves as a phenomenological proxy for the combined mechanical connectivity arising from chain entanglements and crystalline domains—both of which degrade as hydrolysis reduces molecular weight.

2.2 Material-degradation module

Water absorbed by the hydrophilic polymer swells the network, and this swelling in turn accelerates the hydrolysis that cleaves the polymer backbone. We treat the swelling ratio as quasi-steady—at each instant it is set by the current network-integrity density—and rising as network integrity is lost (Flory and Rehner, 1943,?; Peppas and Merrill, 1977; Anseth et al., 1996):

$$q = Q_0 \left[1 + \sigma(1 - \rho_x)\right], \tag{1}$$

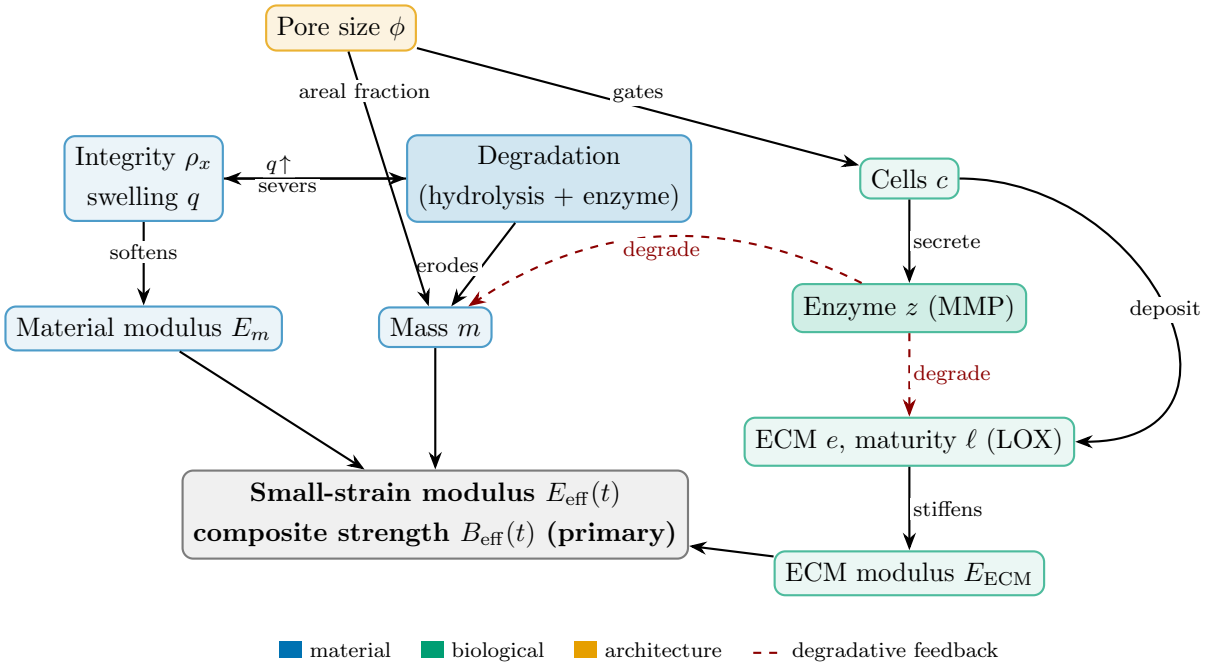

Figure 1: Coupling structure of the implant–tissue system. Solid arrows are constructive couplings; red dashed arrows are degradative feedback. A falling material branch and a rising tissue branch combine into the composite strength B_{eff} (primary) and small-strain modulus E_{eff}.

where q is the swelling ratio (swollen to dry volume), ρ_x is the network-integrity density, Q_0 is the reference (dry-state) swelling, and σ sets how strongly swelling responds to network-integrity loss. Both q and ρ_x then evolve in time as degradation proceeds. The hydrolysis rate k_h grows with swelling (Göpferich, 1996; Metters et al., 2000),

$$k_h = k_{h0}\,\frac{q}{q_{\text{ref}}}, \tag{2}$$

where k_{h0} is the intrinsic hydrolysis rate and $q_{\text{ref}} = Q_0$ is a fixed reference swelling, so the baseline rate is k_{h0}.

The remaining polymer mass $m(t)$ then decreases through hydrolysis and through enzymatic erosion by MMP, the latter following Michaelis–Menten kinetics (Lutolf et al., 2003; Patterson and Hubbell, 2010):

$$\frac{dm}{dt} = -k_h\, m \;-\; \frac{k_{\text{enz}}\, z\, m}{K_m + m}, \tag{3}$$

where k_h is the hydrolysis rate of Eq. (2), z is the MMP concentration, k_{enz} is the enzyme catalytic rate constant, and K_m is the Michaelis constant—the substrate level at which the enzymatic reaction runs at half its maximum rate. The first term is hydrolytic loss (first order in the remaining mass); the second is enzymatic erosion that saturates when substrate is abundant.

The network integrity ρ_x can fall faster than the mass, because a single chain scission can reduce

several connectivity points. We write

$$\frac{d\rho_x}{dt} = -\alpha_x\, k_h\, \rho_x \;-\; \frac{\beta_{\text{enz}}\, k_{\text{enz}}\, z\, \rho_x}{K_m + \rho_x}, \tag{4}$$

where $\alpha_x > 0$ is the fragility—of order unity, so that network integrity is lost at about the same rate as mass (faster when $\alpha_x > 1$)—and β_{enz} scales the enzyme's access to the network; the remaining symbols are as in Eq. (3). For a thin, porous mesh we adopt the standard simplifications of pseudo-first-order scission and omit autocatalysis by acidic products, which diffuse out before catalysing further scission (Vert et al., 1992; Grizzi et al., 1995; Ford Versypt et al., 2013).

2.3 Tissue-integration module

Mesh pore size gates whether cells can migrate into the construct. We model the infiltration activity s_{eff} with a Hill function of the pore size (Hollister, 2005):

$$s_{\text{eff}} = s_b + (1 - s_b)\, \frac{\phi^n}{\phi^n + \phi_c^n}, \tag{5}$$

where ϕ is the pore size, s_b a baseline surface ingrowth (cells on the outer face), ϕ_c the pore size at half-maximum infiltration, and n the Hill exponent setting the sharpness of the transition. Below ϕ_c, ingrowth is strongly suppressed. Fibroblasts then proliferate logistically to a pore-gated carrying capacity,

$$\frac{dc}{dt} = r_c\, c\Big(1 - \frac{c}{K_{c,\text{eff}}}\Big) s_{\text{eff}} - d_c\, c, \qquad K_{c,\text{eff}} = K_c(0.5 + 0.5\, s_{\text{eff}}), \tag{6}$$

where c is the cell density, r_c the proliferation rate, $K_{c,\text{eff}}$ the pore-gated carrying capacity (with K_c its maximum), and d_c the death rate; because $K_{c,\text{eff}}$ itself rises with s_{eff}, architecture feeds back into biology.

Cells deposit collagen—which MMP in turn degrades—and secrete MMP and lysyl oxidase (LOX), the enzyme that crosslinks and stiffens the deposited collagen (Visse and Nagase, 2003; Tomasek et al., 2002; Kagan and Li, 2003):

$$\frac{de}{dt} = \beta_e\, c\Big(1 - \frac{e}{K_e}\Big) - \delta_e\, z\, e, \tag{7}$$

$$\frac{dz}{dt} = \beta_z\, c - \delta_z\, z, \tag{8}$$

$$\frac{d\ell}{dt} = r_\ell\, e(1 - \ell) - d_\ell\, \ell, \tag{9}$$

where e is the deposited collagen density, z the MMP concentration, ℓ the collagen maturity, β_e the secretion rate, K_e the ECM carrying capacity, δ_e and δ_z the enzymatic-loss and enzyme-turnover rates, and r_ℓ, d_ℓ the maturity build-up and decay rates. MMP is thus a double-edged host response: it remodels the matrix but also attacks both the implant and the new tissue.

2.4 Constitutive laws

The small-strain modulus of the degrading polymer combines three effects: rubber elasticity (stiffness proportional to network-integrity density), Flory–Rehner swelling-softening (a swollen network is softer, $\propto q^{-1/3}$), and a gel-point collapse as the network loses spanning connectivity (Flory and Rehner, 1943; Anseth et al., 1996):

$$E_m = E_{m0}\,\rho_x \Big(\frac{q_{\mathrm{ref}}}{q}\Big)^{1/3} G, \qquad G = \frac{1}{1+\exp[(\rho_g-\rho_x)/w_g]}. \tag{10}$$

Here E_m is the material modulus, E_{m0} its reference value, q_{ref}/q the swelling-softening factor, and G the gel-point collapse: $G \approx 1$ while the network is well connected ($\rho_x \gg \rho_g$) but falls sharply once ρ_x drops below the gel point ρ_g, over a width set by w_g. The modulus law borrows the rubber-elasticity and Flory–Rehner forms from crosslinked-network theory; applied to a semicrystalline thermoplastic they are phenomenological—capturing the qualitative stiffness loss with degradation rather than its detailed micromechanics.

The intrinsic modulus of the deposited collagen reflects that a collagen gel is a semiflexible polymer network whose stiffness rises with concentration ($E \propto c^2$), stiffens further as LOX matures it, and bears no load until it percolates (MacKintosh et al., 1995; Storm et al., 2005; Raub et al., 2008):

$$E_{\mathrm{ECM}} = E_{e0}\,e\,(1+\eta\ell)\,P, \qquad P = \frac{1}{1+\exp[(e_g-e)/w_e]}, \tag{11}$$

where E_{ECM} is the ECM modulus, E_{e0} its scale, e the collagen concentration, η the maturity stiffening, ℓ the maturity, and P the collagen percolation gate (the tissue-side analogue of G), which collapses below the collagen gel point e_g over a width w_e.

2.5 Composite laws and the two metrics

How much of the construct is degrading material and how much is new tissue is set by two volume fractions. The material volume fraction is

$$\phi_m = \phi_{m0}\,m, \qquad \phi_{m0} = \phi_{m0,\max}\,\frac{2}{1+\phi}, \tag{12}$$

where ϕ_m is the current material volume fraction, ϕ_{m0} its initial value (denser for small pores, lighter for large pores, with maximum $\phi_{m0,\max}$), and m the remaining mass—so ϕ_m decays as the polymer resorbs. The tissue fill fraction is simply the deposited collagen e, which grows from 0 to replace the lost material.

The composite modulus is the volume-weighted sum of the two phases, taken in the Voigt (parallel, upper-bound) limit (Hashin and Shtrikman, 1963; Halpin and Kardos, 1976; Cox, 1952):

$$E_{\mathrm{eff}} = \phi_m\,E_m + e\,E_{\mathrm{ECM}}, \tag{13}$$

Table 1: Parameters of the reduced model (time in weeks). A = literature-anchored; E = estimated range (Table 2); F = fitted to Phasix; D = design variable (swept in the design maps). The mechanical floor is $S_{\min} = 0.35$ and the simulation horizon is $T = 62$ weeks.

Sym.	Meaning	Value	Src.	Sym.	Meaning	Value	Src.
k_{h0}^*	hydrolysis rate	0.025	F,D	k_{enz}, K_m	enzymatic rate, MM	$0.04, 0.10$	A
α_x^*	integrity fragility	0.99	F,D	$\beta_{\text{enz}}, \sigma$	enz. access, swell. resp.	$0.6, 0.9$	A
Q_0^*	swelling ratio	1.5	A,D	ϕ^*	pore size	1.0	D
ϕ_c, n, s_b	pore threshold/exp.	$0.55, 2.0, 0.2$	A	$\phi_{m0,\max}$	max mat. fraction	0.60	A
E_{m0}, B_{m0}	modulus/strength scale	$1.0, 1.0$	A	ρ_g, w_g	polymer gel pt/width	$0.15, 0.05$	A
e_g, w_e	collagen gel pt/width	$0.15, 0.05$	A,E	r_c	cell proliferation	0.40	E
K_c, d_c	carry. cap., death	$0.90, 0.05$	E	β_e	ECM secretion	0.85	E
K_e, δ_e	ECM cap., enz. loss	$1.0, 0.18$	E	β_z, δ_z	MMP secre./turn.	$0.35, 0.90$	E
r_ℓ, d_ℓ	maturation rate/decay	$0.03, 0.015$	E	η	maturity stiffening	0.90	E
E_{e0}	ECM modulus scale	0.182	E	B_{e0}	tissue strength scale	≈ 0.24	F

where E_{eff} is the composite modulus, $\phi_m E_m$ the falling material contribution, and $e\,E_{\text{ECM}}$ the rising tissue contribution. This modulus governs the comfort axis (matching the surrounding tissue stiffness).

For the recurrence axis we form the analogous composite strength. The material's intrinsic strength b_m differs from its modulus E_m by carrying an extra factor of the remaining mass m: degradation embrittles the surviving polymer, so its strength falls faster than its modulus,

$$b_m = B_{m0}\, m\, \rho_x\, G, \qquad b_{\text{ECM}} = B_{e0}\, e\, (1 + \eta\ell)\, P, \tag{14}$$

$$B_{\text{eff}} = \phi_m\, b_m + e\, b_{\text{ECM}}, \tag{15}$$

where b_m and b_{ECM} are the intrinsic strengths of the material and tissue (compare E_m, E_{ECM}), B_{m0} and B_{e0} their scales, and B_{eff} the Voigt composite strength. The tissue strength b_{ECM} reuses the same drivers as E_{ECM} (concentration e, maturity ℓ, percolation P). Because e enters both as the fill fraction and as the concentration inside E_{ECM} (and b_{ECM}), the tissue contribution scales as e^2, matching the collagen-gel law.

Finally, to compare designs on a common scale we normalise to fixed references:

$$S_E = \frac{E_{\text{eff}}}{E_{\text{ref}}}, \qquad S_B = \frac{B_{\text{eff}}}{B_{\text{ref}}}, \qquad E_{\text{ref}} = \phi_{m0,\max} E_{m0}, \quad B_{\text{ref}} = \phi_{m0,\max} B_{m0}, \tag{16}$$

where S_E and S_B are the normalised stiffness and strength and E_{ref}, B_{ref} the acute values of a dense reference mesh. Both S_E and S_B start at the acute value and trace a valley as the load is handed off; we denote their minima $R_B = \min_t S_B$ (the strength valley) and $R_E = \min_t S_E$ (the stiffness valley), the design criteria studied below.

3 Parameterization and calibration

3.1 Treatment strategy

The model contains roughly 28 parameters. Not all of them can—or need to—be precisely identified; fitting all to a single dataset would be underdetermined. Instead we assign values in four ways.

Literature-anchored parameters with direct experimental precedent (gel points, Michaelis constants, pore thresholds) are fixed at published values. *Literature-estimated* biological rate constants (cell proliferation, ECM secretion, MMP kinetics) are known only within plausible ranges; we define these ranges (§3.4) and sweep them later rather than fitting. The hydrolysis rate k_{h0} and the fragility α_x are *fitted* to the Mw-retention data, and the tissue-strength scale B_{e0} to the burst-strength data (§3.3); the tissue-modulus scale E_{e0} and the maturation rate r_ℓ are estimated from literature ratios and timescales (§3.3). Finally, the material and architecture parameters the designer controls (k_{h0}, swelling Q_0, pore size ϕ, fragility α_x) serve as *design variables* swept in the design maps (§4.4). Note that k_{h0} and α_x play dual roles: fitted for the calibrated baseline, swept for the design exploration; Q_0 likewise has a literature-anchored baseline (1.5) for the Phasix calibration and is swept as a design variable, while ϕ is a pure design variable (nominal 1.0).

3.2 Literature-anchored parameters

The gel-point threshold ρ_g and width w_g for the polymer network, and the analogous e_g and w_e for collagen, are set near the percolation threshold typical of lightly crosslinked gels (ρ_g=0.15, w_g=0.05; e_g=0.15, w_e=0.05) (Anseth et al., 1996; Flory and Rehner, 1943). The Michaelis constant K_m=0.10 and the Hill parameters for pore gating (ϕ_c=0.55, n=2) are set at representative values for enzyme–substrate and cell–pore interactions (Lutolf et al., 2003; Hollister, 2005). The swelling parameters Q_0=1.5 and σ=0.9 reflect a moderately hydrophilic polyester (Peppas and Merrill, 1977). These values are collected with the others in Table 1.

3.3 Calibration to Phasix (P4HB)

The model is calibrated to the porcine Phasix (P4HB) dataset of Deeken and Matthews (2013), which reports molecular-weight (Mw) retention, measured by gel-permeation chromatography, and composite ball-burst strength, each over 52 weeks, the latter normalised to the acute mesh-only value (≈ 487 N). Because P4HB erodes in the bulk—chains cleave throughout the material before fragments dissolve—Mw falls well before any mass is lost and is the cleanest descriptor of structural degradation; we identify Mw retention with the network integrity ρ_x.

The hydrolysis prefactor k_{h0} and the fragility α_x are obtained by nonlinear least squares against Mw retention, and the tissue-strength scale B_{e0} against the burst data through the composite strength retention $B_{\text{eff}}(t)/B_{\text{eff}}(0)$—the quantity a rupture test measures. The B_{e0} fit is evaluated at the rep-

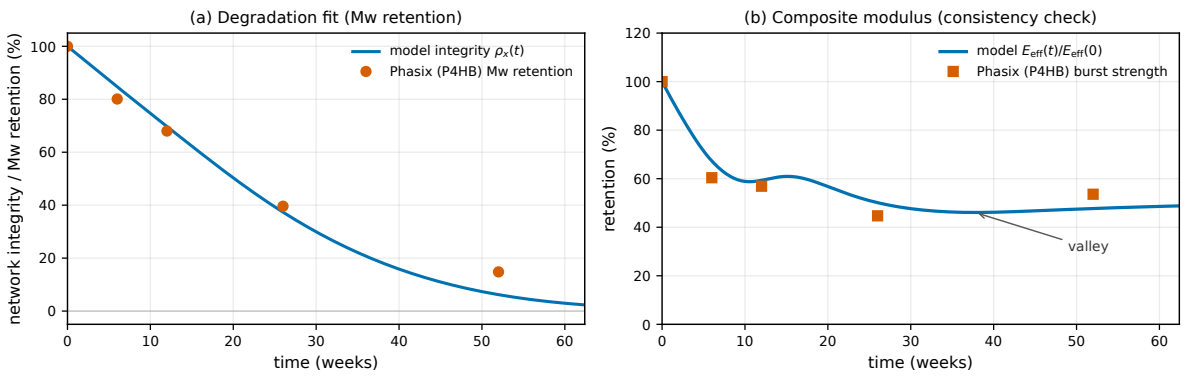

Figure 2: Calibration to Phasix (P4HB) data (Deeken and Matthews, 2013). (a) Degradation: network integrity (model ρ_x) fitted to Mw retention (RMSE ≈ 4.4 pp). (b) Strength: composite strength retention $B_{\text{eff}}(t)/B_{\text{eff}}(0)$ fitted to ball-burst retention (RMSE ≈ 3.0 pp). The green triangle marks the strength valley (≈ 32 wk).

resentative values of the tissue-kinetic parameters, whose uncertainty is propagated through the sensitivity analysis and robust-design sweep (§3.4). The two fits reproduce their respective signals to 4.4 and 3.0 percentage points RMSE (Fig. 2); the fitted values are listed in Table 1. The recovered hydrolysis rate ($k_{h0} = 0.025$ wk^{-1}) is consistent with P4HB's slow in-vivo absorption ($\sim$12–18 months) (Martin and Williams, 2003), and the near-unity fragility places network-integrity loss and mass loss on comparable timescales.

Two parameters that lack a direct measurement are assigned from the literature and propagated as uncertainties: E_{e0} from the ratio of typical remodelling-tissue modulus (5–30 MPa) to the P4HB modulus ($\sim$70 MPa), and the maturation rate r_ℓ from wound-healing kinetics—collagen is laid down within weeks, but crosslinking and remodelling raise tensile strength over many months, approaching the mature value only near one year (Gurtner et al., 2008). Under this calibration the composite strength reaches a transient minimum near 32 weeks as the load shifts from the resorbing polymer to the integrating tissue, and recovers partially thereafter (Fig. 2b); we analyse this minimum—the strength valley—in §4.1.

3.4 Uncertain biological parameters

The biological rate constants—cell proliferation r_c and death d_c with the carrying capacity K_c, collagen secretion β_e and ECM capacity K_e, ECM enzymatic loss δ_e, MMP secretion β_z and turnover δ_z, LOX maturation r_ℓ and decay d_ℓ, maturity stiffening η, and the collagen gel point e_g and width w_e—cannot be independently measured for a specific patient or mesh. Rather than fitting them, we assign each a plausible range based on literature estimates of fibroblast doubling times (1–4 wk), collagen deposition rates, and MMP/LOX kinetics (Table 2). These ranges define the biological uncertainty explored later: a global sensitivity analysis (§4.2) shows that the parameters hardest to

Table 2: Plausible ranges for the uncertain biological parameters (from literature estimates; used in sensitivity analysis and robust design).

Sym.	Meaning	Range	Sym.	Meaning	Range
r_c	cell proliferation	0.20–0.80	β_z	MMP secretion	0.10–0.80
K_c	carrying capacity	0.50–1.20	δ_z	MMP turnover	0.30–2.00
d_c	cell death	0.01–0.10	r_ℓ	LOX maturation	0.01–0.08
β_e	ECM secretion	0.30–1.50	d_ℓ	maturity decay	0.01–0.10
K_e	ECM capacity	0.80–1.20	η	maturity stiffening	0.30–2.00
δ_e	ECM enzymatic loss	0.05–0.40	e_g	collagen gel pt	0.05–0.25
			w_e	gel-pt width	0.02–0.10

identify are also the least influential on the valley metric, and a robust-design map finds material designs that remain safe across the full ranges.

3.5 Design variables

The material design parameters—the hydrolysis rate k_{h0} (polymer chemistry), the swelling Q_0 (hydrophilicity), the pore size ϕ (architecture), and the fragility α_x—are the levers a mesh designer can control. They are marked with * in Table 1 and swept in the design maps (§4.4) to map the design space and locate the safe-design window.

4 Results

We first establish the baseline dynamics of the calibrated model and then use a global sensitivity analysis to triage the parameters that govern the strength valley—distinguishing the few that must be analysed in detail from the many whose precise value is immaterial.

4.1 Baseline dynamics and the strength valley

Integrating the calibrated model over the $T = 62$-week horizon, the polymer mass m and network integrity ρ_x fall as hydrolysis and enzymatic attack proceed, while the tissue fill fraction e and collagen maturity ℓ rise as fibroblasts deposit and crosslink new matrix. The composite strength $B_{\text{eff}}(t) = \phi_m b_m + e\, b_{\text{ECM}}$ tracks the handoff between these two arms: it begins polymer-dominated, descends as the resorbing material loses load-bearing capacity faster than tissue accrues, passes through a minimum—the *strength valley*—and recovers as the maturing tissue assumes the load (Fig. 3). At the calibrated baseline the valley is modest, $R_B = \min_t B_{\text{eff}}/B_{\text{ref}} \approx 0.48$ near 32 weeks, and the composite stays above the rupture floor $S_{\min} = 0.35$ throughout, consistent with the maintained strength that Phasix shows clinically. The small-strain stiffness margin R_E dips lower still, to about

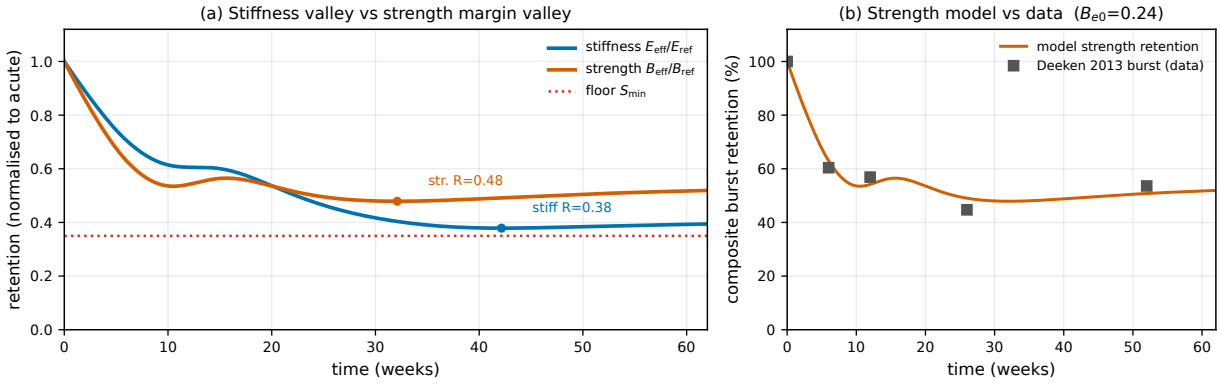

Figure 3: The strength valley at the calibrated baseline. (a) Strength margin $B_{\text{eff}}/B_{\text{ref}}$ (primary) and the small-strain stiffness margin $E_{\text{eff}}/E_{\text{ref}}$ over the 62-week horizon, with the rupture floor $S_{\min}$. The strength margin reaches a shallow minimum $R_B \approx 0.48$ near 32 weeks and recovers as tissue matures; the stiffness margin dips lower still. (b) Model strength retention versus the Phasix ball-burst data (Deeken and Matthews, 2013).

0.38 near 42 weeks; but recurrence is a tearing (strength) failure rather than a softening one, so we take R_B as the primary metric—the rupture floor is a strength criterion, and stiffness, plotted against it only for scale, governs comfort rather than rupture.

4.2 Global sensitivity and parameter triage

To decide which parameters merit detailed study and which may be held at representative values, we rank their influence on *both* failure metrics by global sensitivity analysis. We draw $N = 2500$ Latin-hypercube samples over all 28 parameters and, for each draw, evaluate both the strength valley R_B (rupture) and the stiffness valley R_E (the foreign-body sensation tied to stiffness). The biological parameters vary over their Table 2 ranges and the material/design parameters over plausible polymer and architecture ranges; the tissue-strength scale B_{e0} is held fixed at its calibrated value (a fitted normalisation whose uncertainty is an identifiability question we address separately). We measure each parameter's monotonic influence by the partial rank correlation coefficient (PRCC; Marino et al., 2008), which partials out the other parameters. We triage *each metric independently* into three tiers—High ($|\text{PRCC}| \geq 0.30$, $p < 0.01$), Medium (0.10–0.30), and Negligible (< 0.10)—and act on the tiers uniformly: High-tier parameters receive a dedicated one-at-a-time sweep and enter the design/robustness sweeps; Medium-tier parameters are propagated as uncertainty (varied over their ranges in the robust-design sweep, their direction of effect noted) but are not studied one at a time; Negligible-tier parameters are fixed at representative literature values and not varied further. (The design variables $k_{h0}, Q_0, \alpha_x, \phi$ anchor the design maps regardless of tier—ϕ is only Medium by PRCC because its effect is non-monotonic, yet it is swept as a design lever.) We treat strength as the primary metric and present its triage first, then stiffness.

Table 3: Strength triage (PRCC of R_B, $N = 2500$). High: $|\text{PRCC}| \geq 0.30$ ($p < 0.01$); Medium: 0.10–0.30; Negligible: < 0.10. Disposition: High → one-at-a-time sweep and enters the design/robustness sweeps; Medium → varied as uncertainty in the robust-design sweep; Negligible → fixed at literature values. The four design variables ($k_{h0}, Q_0, \alpha_x, \phi$) anchor the design maps regardless of tier.

Tier	Parameters	Disposition
High (5)	k_{h0}, Q_0, α_x (degradation); r_c, β_e (regeneration)	OAT + sweeps
Medium (9)	$\sigma, d_c, \phi_c, \phi_{m0,\max}, K_e, \phi, \beta_z, \rho_g, \delta_z$	robust-design
Negligible (12)	$w_e, \delta_e, e_g, k_{\text{enz}}, \eta, n, r_\ell, K_c, d_\ell, w_g, K_m, \beta_{\text{enz}}$	fixed (lit.)

Strength valley R_B. Five parameters dominate the strength valley (Fig. 4a, Table 3): on the degradation side the hydrolysis rate k_{h0} (-0.92), the swelling Q_0 (-0.76), and the crosslink fragility α_x (-0.61); on the regeneration side the cell proliferation r_c ($+0.73$) and collagen secretion β_e ($+0.69$). Faster degradation deepens the valley (negative PRCC) and faster tissue build-up shallows it (positive): the valley is a race between resorption and integration. The material/design group accounts for 0.66 of the variance in R_B and biology for 0.17 (full-model $R^2 = 0.82$), so the outcome is governed mainly by chemistry and architecture a designer can control, with the two tissue-secretion rates as the principal biological counterweights. A Medium tier of nine parameters ($|\text{PRCC}| = 0.11$–0.22: $\sigma, d_c, \phi_c, \phi_{m0,\max}, K_e, \phi, \beta_z, \rho_g, \delta_z$) is carried as uncertainty below, and twelve are Negligible—the enzyme Michaelis–Menten trio ($k_{\text{enz}}, K_m, \beta_{\text{enz}}$), the gel-point and percolation widths (w_g, e_g, w_e), the maturity triplet (r_ℓ, d_ℓ, η), and δ_e, K_c, n—confirming the valley is insensitive to the precise shape of these transitions. (E_{m0}, E_{e0} do not enter B_{eff} and are excluded from the strength triage; r_ℓ was sampled over its slow wound-healing range (0.01–0.08) and is Negligible within it—it must be slow to reproduce the late valley, but its exact value then barely moves R_B.)

Stiffness valley R_E. The stiffness valley is governed by the same five levers—k_{h0} (-0.88), Q_0 (-0.72), α_x (-0.61), r_c ($+0.64$), β_e ($+0.61$)—now joined by the tissue-modulus scale E_{e0} ($+0.55$), which is inert for strength (Fig. 4b, Table 4). Stiffness is therefore driven by the same degradation–regeneration balance as strength, plus the modulus of the deposited tissue. A Medium tier of seven ($\sigma, E_{m0}, d_c, \phi_c, \phi_{m0,\max}, K_e, \beta_z$) carries secondary influence—notably E_{m0} (-0.22), whose sign is negative because raising the material-modulus scale raises the reference faster than it helps at the tissue-dominated valley—and fifteen are Negligible. The material/design group accounts for 0.62 of the variance in R_E and biology for 0.21 (full-model $R^2 = 0.81$). On stiffness the pore size ϕ reads PRCC ≈ 0 ($+0.002$) because stiffness has an interior pore optimum that a monotonic PRCC cannot see (on strength ϕ is only Medium, $+0.13$, for the same reason); in both cases ϕ is swept separately as a design variable rather than read off this ranking.

Synthesis. The two failure modes share their five governing levers (k_{h0}, Q_0, α_x on the degradation side, r_c, β_e on the regeneration side), so design choices that protect strength also protect stiffness

Table 4: Stiffness triage (PRCC of R_E, $N = 2500$). Same thresholds and dispositions as Table 3. $\phi^\dagger$ is Negligible by PRCC only because its effect is non-monotonic (interior optimum); it is swept separately as a design variable.

Tier	Parameters	Disposition
High (6)	$k_{h0}, Q_0, \alpha_x, r_c, \beta_e, E_{e0}$	OAT + sweeps
Medium (7)	$\sigma, E_{m0}, d_c, \phi_c, \phi_{m0,\max}, K_e, \beta_z$	robust-design
Negligible (15)	$\rho_g, \delta_z, \eta, \delta_e, e_g, w_e, d_\ell, K_c, k_{\text{enz}}, r_\ell, n, K_m, w_g, \beta_{\text{enz}}, \phi^\dagger$	fixed (lit.)

and the foreign-body sensation it governs; stiffness alone additionally depends on the modulus scales E_{e0}, E_{m0}. In both valleys the material/design group dominates the variance over biology, so the conclusions rest on parameters that are measurable or designable. The analyses that follow accordingly sweep the High-tier parameters one at a time, anchor the two-dimensional design maps on the design variables $(k_{h0}, Q_0, \alpha_x, \phi)$, propagate the Medium tier as uncertainty in a robust-design sweep, and hold the Negligible tier at representative literature values.

4.3 One-at-a-time sweeps of the governing levers

We probe the mechanism by sweeping each High-tier parameter across its range (all others at the calibrated baseline), taking the union of the strength and stiffness High tiers—six parameters—and recording both valleys (Fig. 5). The degradation levers deepen both valleys monotonically: hydrolysis carries the strength margin below the floor beyond $k_{h0} \approx 0.040$ wk^{-1} (the calibrated 0.025 is well below this limit), swelling beyond $Q_0 \approx 2.4$, while crosslink fragility α_x alone stays above the floor across its range. The regeneration levers act in the opposite direction with saturation: cell proliferation must exceed $r_c \approx 0.21$ and collagen secretion $\beta_e \approx 0.31$ for the strength margin to clear the floor. The two arms are thus asymmetric—degradation sets a hard upper rate, regeneration a soft lower threshold—the quantitative form of the matched-degradation/integration principle. The stiffness modulus scale E_{e0}, finally, moves the stiffness valley across a wide range ($R_E \approx 0.21$–0.74) while leaving the strength valley flat ($R_B \approx 0.48$), confirming at the mechanism level that it governs comfort, not rupture.

4.4 Safe-design maps over the design variables

Figure 6 maps the strength valley over two design-variable planes. In the hydrolysis–pore plane ($k_{h0} \times \phi$), 34% of the swept combinations stay above the floor. The safe region is a band of slow-to-moderate hydrolysis and mid-range pore size: pore size has an interior optimum near $\phi \approx 1$—too small and cell ingrowth is blocked (a deep valley), too large and the material is too sparse to bear the load—and faster hydrolysis erodes the window from above. The swelling–fragility plane ($Q_0 \times \alpha_x$) is safer (68%): only the corner of high swelling together with high fragility fails. Only two planes

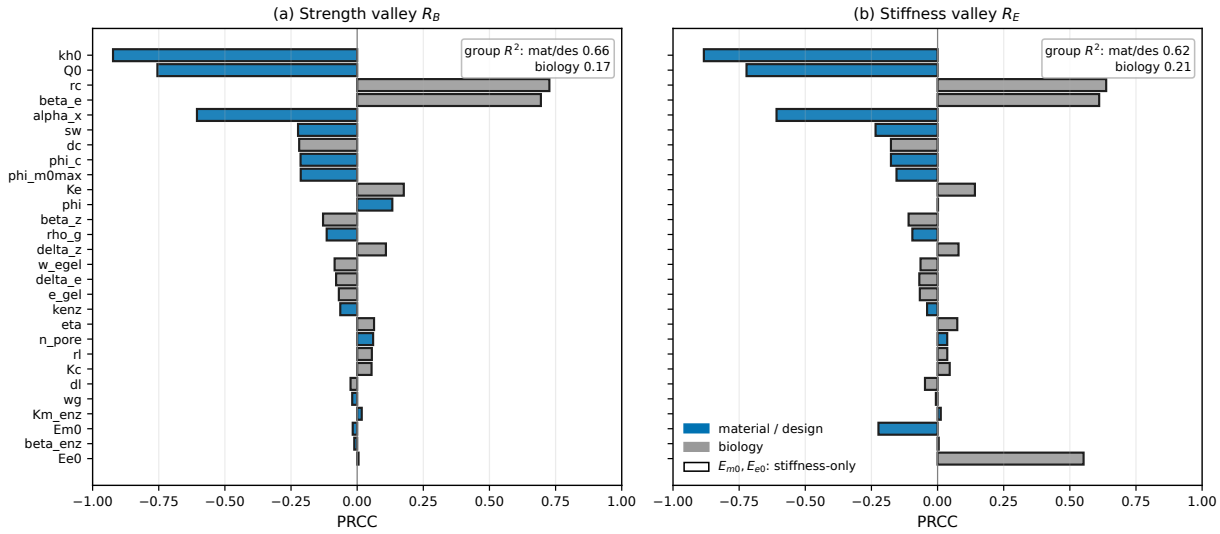

Figure 4: Global sensitivity of both failure metrics (PRCC; $N = 2500$ shared Latin-hypercube samples over 28 parameters), the two panels in the same parameter order (sorted by $|R_B$ PRCC$|$) for direct comparison. (a) Strength valley R_B; (b) stiffness valley R_E. Blue = material/design, grey = biology; the outlined bars (E_{m0}, E_{e0}) enter stiffness only and are ≈ 0 for strength. Both metrics share the top five drivers $(k_{h0}, Q_0, \alpha_x, r_c, \beta_e)$; stiffness additionally ranks E_{e0} high. Group variance explained: strength material/design 0.66, biology 0.17; stiffness 0.62, 0.21.

are shown because the four design variables have just two qualitative pairwise structures: ϕ alone is non-monotone (its interior pore optimum), while k_{h0}, Q_0, α_x are monotone, so every pair is either a pore-optimum plane (with ϕ) or a monotone chemistry plane (without it); one of each is representative—the other four share these two shapes though their safe fractions differ quantitatively (30–88%; Appendix A)—and the full four-dimensional space matters more than any single slice. That space, estimated by Monte Carlo over all four design variables (biology at baseline), has a safe volume of $\approx$21% (Fig. 7)—below the 34% and 68% of the two slices, since all four levers must jointly lie in their safe sub-ranges. Because stiffness shares the same five levers, this window protects both failure modes, so we anchor the design analysis on the strength criterion R_B.

4.5 Robustness to biological uncertainty

The maps above hold the biology at its central values. To test robustness we re-sweep the $k_{h0} \times \phi$ plane while sampling the Medium- and High-tier biology (Negligible tier fixed) over their ranges, taking the near-worst-case (5th-percentile) R_B at each design point (Fig. 8). The nominal window (the same $k_{h0} \times \phi$ plane as Fig. 6; 33% safe on the coarser grid used here for the Monte Carlo, $\approx$34% on the fine grid) collapses: under adverse tissue kinetics the 5th-percentile map is everywhere below the floor (0% safe). This is not a numerical artefact but a direct consequence of the biological ranges that the OAT thresholds diagnose: they admit tissue integration slow enough (r_c down to

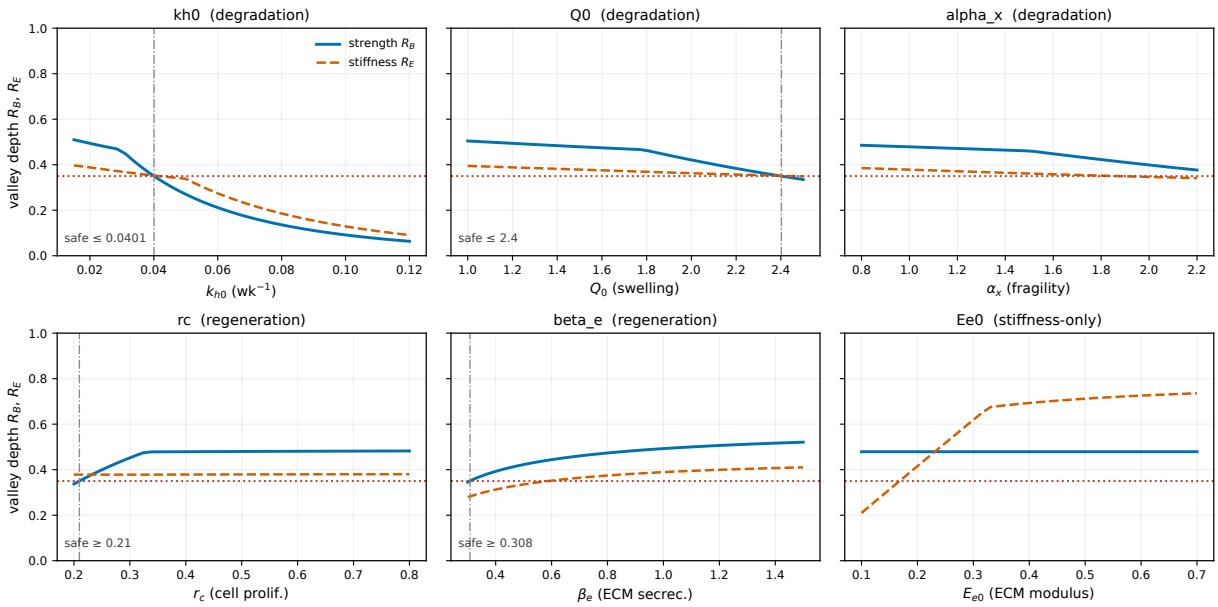

Figure 5: One-at-a-time sweeps of the High-tier parameters (each varied across its range, others at baseline). Solid = strength valley R_B, dashed = stiffness valley R_E, dotted horizontal = rupture floor $S_{\min}$. (Row 1) Degradation levers k_{h0}, Q_0, α_x deepen both valleys; the dash–dot line marks where R_B crosses the floor ($k_{h0} \approx 0.040$, $Q_0 \approx 2.4$). (Row 2) Regeneration levers r_c, β_e shallow the strength valley with saturation; E_{e0} moves only stiffness (R_B flat).

0.2, β_e to 0.3, both below their safe thresholds) that no mesh chemistry or architecture can keep the regeneration arm abreast of resorption.

The implication is clinical rather than merely pessimistic. When host tissue integration is poor, no choice of mesh alone can prevent a strength failure: the construct's integrity is co-determined by the regeneration arm, which the mesh does not control. A subset of recurrences may therefore reflect inadequate tissue integration rather than a deficiency of the mesh—failures of the biological arm, not the material—which is consistent with the clinical observation that many recurrences lack an identifiable mesh defect. This redirects part of the recurrence problem away from mesh design and toward the tissue side: measures that accelerate or augment integration, from coatings that favour fibroblast activity and growth-factor delivery to the correction of patient factors that impair healing (diabetes, smoking, malnutrition), become complementary levers, since the model shows they can move a design from unsafe to safe where chemistry alone cannot. The matched-degradation/integration principle thus operates on both arms: a safe repair needs the mesh slow enough *and* the tissue fast enough.

4.6 Structural uncertainty: mixing-rule bounds

The composite law $B_{\text{eff}} = \phi_m b_m + e\, b_{\text{ECM}}$ is a Voigt (parallel) blend—an *upper* bound on the composite strength—so every result in §4.3–4.5 is an optimistic estimate. We bracket it with the lower bound

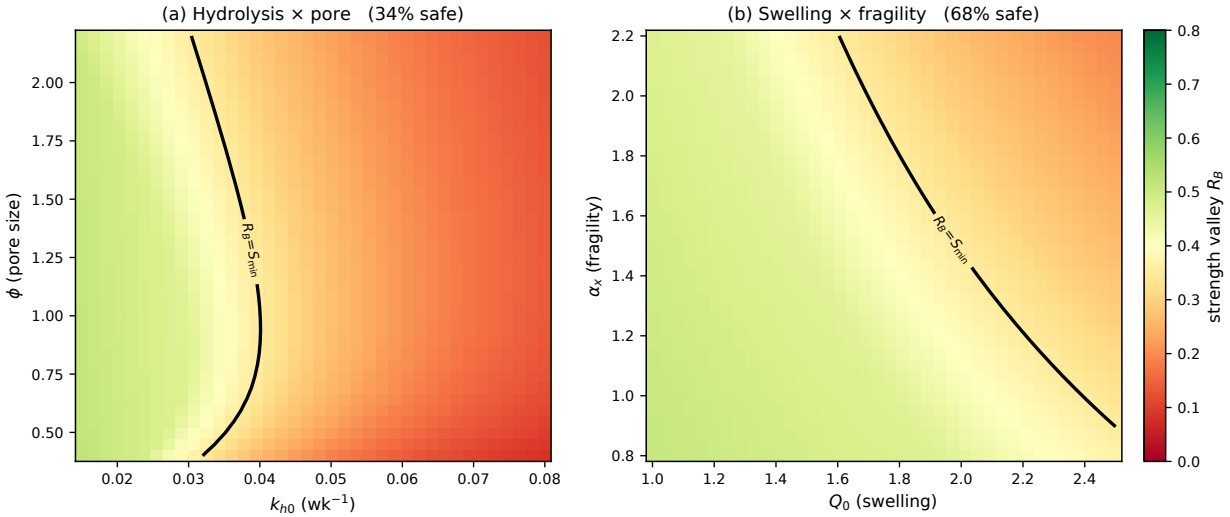

Figure 6: Strength safe-design windows (R_B; black contour = rupture floor $S_{\min}$). (a) Hydrolysis $k_{h0}\times$ pore size ϕ: 34% of designs safe; pore size has an interior optimum near $\phi \approx 1$. (b) Swelling $Q_0\times$ fragility α_x: 68% safe; only the high-swelling, high-fragility corner fails.

by re-evaluating the strength valley under three mixing rules on the percolation-gated load-bearing skeleton (material above the gel point and tissue above the collagen gel point; without this gating the lower bound degenerates toward zero on so soft a composite). At the calibrated baseline the valley depths are 0.48 (Voigt, upper), 0.16 (Hashin–Shtrikman lower), and 0.09 (Reuss) (Fig. 9a,b): the bracket $[0.16, 0.48]$ *straddles* the rupture floor $S_{\min} = 0.35$.

The safety margin is therefore *conditional on the mixing rule*. Under the conservative lower bound the baseline sits well below the floor, and the $k_{h0} \times \phi$ design window that §4.4 locates under Voigt is closed: under the Hashin–Shtrikman lower bound no design in the swept space is safe (Fig. 9c). The qualitative conclusions of §4.3–4.5—the shared governing levers, the matched-degradation/integration principle, and the co-determination of safety by tissue integration—do not depend on the mixing rule, but the quantitative margin does. The honest position is the bracket itself, with the rupture floor lying inside it: a favourable Voigt estimate is necessary but not sufficient, and the conservative check is that the lower bound also clear the floor—which, for this construct, it does not without either a more favourable composite architecture or a faster tissue response. This is the structural counterpart of §4.5's biological result: the margin is thin in both uncertainty dimensions, and mesh design alone cannot guarantee it.

5 Discussion

The central result of this work is that the mechanical performance of a biodegradable hernia mesh is decided during a transient hand-off period, not at the moment of implantation, and that the

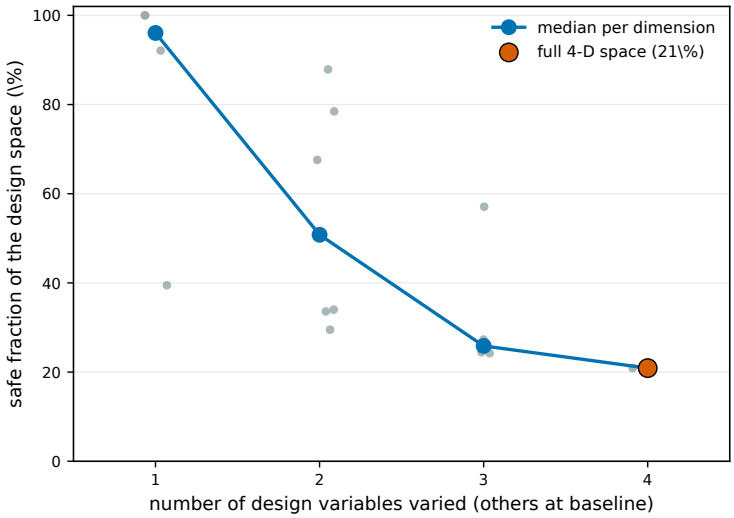

Figure 7: Safe fraction of the design space versus how many of the four design variables are varied (the others held at the calibrated baseline). Grey points: individual subsets (one variable alone, each pairwise slice, each leave-one-out triple); blue line: the median at each dimension; orange point: the full four-dimensional space. Freeing more design levers shrinks the safe set, so the two-dimensional slices of Fig. 6 overestimate safety and the full four-dimensional safe volume is only $\approx$21%.

decisive quantity is a *strength valley*—a transient minimum in the composite strength as the load transfers from the resorbing polymer to the integrating tissue (Fig. 3)—that must stay above the rupture floor throughout. Stiffness, by contrast, traces a deeper, later valley—declining from the polymer-dominated value to a minimum near 42 weeks and recovering toward the tissue value—but because recurrence is a tearing rather than a softening failure, the strength valley remains the binding rupture-risk window. What follows interprets what governs these two trajectories, what the analysis implies for design, and—most importantly—where the safety margin proves thin.

5.1 The strength valley and the matched-rate principle

The valley exists because the polymer forfeits strength faster than the tissue replaces it: there is an interval in which neither phase alone carries the load. Both metrics are met only when degradation and tissue integration proceed at matched rates, formalising the balance long advocated in tissue engineering (Hutmacher, 2001; Drury and Mooney, 2003; Hollister, 2005; Pascual et al., 2012). This rates-matched window, not the initial property, is what a degradable mesh must be designed around. Prior modelling captures only one side of the hand-off: degradation models track the polymer in isolation (Pan et al., 2022; Metters et al., 2000; Göpferich, 1996; Ford Versypt et al., 2013), and tissue-growth models resolve matrix deposition without the replacing mesh (Akalp et al., 2016; Dhote et al., 2013; Chen et al., 2011). Computational growth-and-remodelling frameworks (Emmert et al., 2018) address a related transfer in soft tissues but do not isolate the strength valley of an implant–

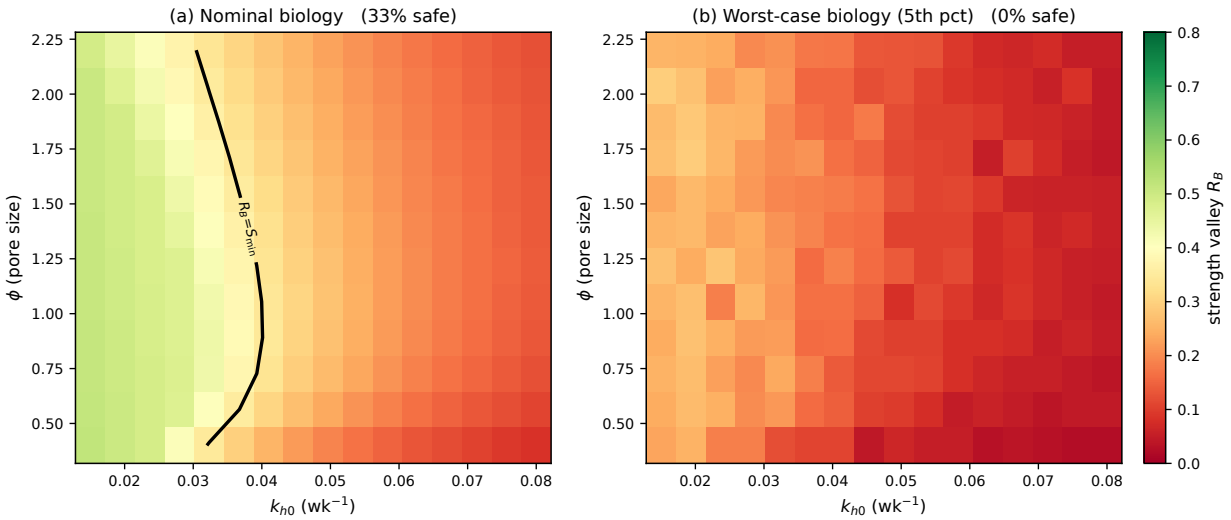

Figure 8: Robustness of the strength safe-design window to biological uncertainty (R_B over $k_{h0} \times \phi$; black contour = floor $S_{\min}$). (a) Nominal (central) biology: 33% of designs safe. (b) Near-worst-case biology (5th percentile over the Medium/High-tier biology): 0% safe—the window collapses when tissue integration is poor, so safety cannot be achieved by mesh design alone.

tissue composite. By coupling both phases into a single composite trajectory calibrated to a real mesh, the present model makes the valley—the operative risk window—explicit and quantitative.

5.2 Shared governing levers and the practical design guidance

Global sensitivity shows that both failure modes run on the same five levers (Fig. 4, Tables 3–4): on the degradation side the hydrolysis rate k_{h0}, the swelling ratio Q_0, and the crosslink-fragility coefficient α_x; on the regeneration side the cell-proliferation rate r_c and the collagen-secretion rate β_e. In both metrics the material/design group explains more variance than the biological group, so the conclusions rest on parameters that are measurable or directly designable. These rankings translate into concrete thresholds from the one-at-a-time sweeps (Fig. 5): $k_{h0} \leq 0.04$, $Q_0 \leq 2.4$, $r_c \geq 0.21$, and $\beta_e \geq 0.31$ keep the valley above the floor, while α_x shows no crossing over its range. The two-dimensional design maps (Fig. 6) locate the safe region: about a third of the $k_{h0} \times \phi$ grid and roughly two-thirds of the $Q_0 \times \alpha_x$ grid are safe, with an optimal pore size $\phi \approx 0.98$. Notably the pore size has near-zero partial-rank correlation because it has an *internal* optimum—a pore too small stifles tissue ingrowth, one too large forfeits strength—so it must be swept directly rather than read off the sensitivity ranking; this non-monotone optimum is consistent with scaffold and pore-size literature (Hollister, 2005; Drury and Mooney, 2003; Bellón et al., 2007; Pascual et al., 2012; Deeken and Lake, 2017). A practical relief for calibration is that the parameters hardest to identify individually—the enzyme Michaelis–Menten constants, the gel-point and percolation widths, and the maturation constants—are also the least influential (Marino et al., 2008), so the design guidance does

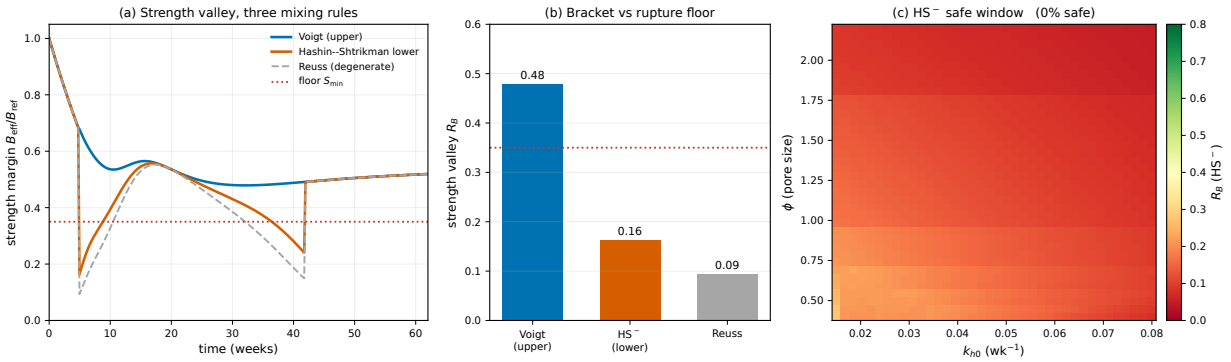

Figure 9: Structural uncertainty of the strength valley under three mixing rules (percolation-gated skeleton). (a) Strength margin over time: Voigt (upper), Hashin–Shtrikman lower, and Reuss, with the rupture floor $S_{\min}$. (b) Valley depths: the bracket $[0.16, 0.48]$ straddles the floor 0.35, so the safety margin is conditional on the mixing rule. (c) The $k_{h0} \times \phi$ design map under the Hashin–Shtrikman lower bound: no design is safe (0%), in contrast to the Voigt window of Fig. 6.

not hinge on their precise values.

5.3 Stiffness, foreign-body sensation, and the shared-lever dividend

Stiffness rides the same five levers, with the deposited-tissue modulus scale E_{e0} (and, through the reference, the material modulus E_{m0}) added independently. Because the two metrics share their drivers, the design choices that protect strength also protect the stiffness that governs foreign-body sensation and chronic discomfort (Deeken and Lake, 2017; Pott et al., 2012; Todros et al., 2015); and because stiffness matching to the surrounding tissue matters for mechanotransduction and constructive remodelling (Engler et al., 2006; Tomasek et al., 2002), a stiffness that approaches the tissue value is not merely comfortable but biologically favourable. The dividend is that a single composite design move—matched-rate degradation on the shared levers—purchases both a rupture-safe and an unobtrusive mesh, rather than trading one against the other.

5.4 Safety is co-determined by the tissue side

The most cautionary result is that the safe window is not determined by mesh design alone. Under nominal biology roughly a third of the design grid is safe, but under the worst-case (5th-percentile) biological draw this collapses to *zero* (Fig. 8): adverse tissue kinetics ($r_c \to 0.2$, $\beta_e \to 0.3$) fall below the one-at-a-time thresholds, so no mesh in the swept space remains safe. The implication is clinical. In patients whose tissue-side conditions are poor—obesity, diabetes, smoking, collagen disorders, or contaminated surgical fields—attention must extend beyond the mesh itself to improving the tissue side, whether by optimising the local wound environment, adjunctive biological support, or staged repair (Deeken and Lake, 2017; Bellón et al., 2007; Fatkhudinov et al., 2018; Heidari et al., 2024;

Gurtner et al., 2008). By the same token, recurrences in such settings need *not* signal mesh failure: a mesh that is safe under favourable biology can be overwhelmed when the tissue cannot integrate fast enough. This reframes a class of recurrences that are otherwise attributed to the implant as tissue-side failures, and it identifies the tissue-secretion rates r_c and β_e as the biological levers most worth measuring and, where possible, supporting.

5.5 Structural uncertainty and the conditional margin

The structural analysis (§4.6) is the second reason the margin is thin. The composite law used throughout §4.3–4.5 is a Voigt blend—an upper bound—and the percolation-gated Hashin–Shtrikman lower bound brackets the strength valley at [0.16, 0.48], which *straddles* the rupture floor $S_{\min} = 0.35$ (Fig. 9). The safety margin is therefore conditional on the mixing rule: under the conservative lower bound the baseline sits below the floor and the design window closes. Voigt is a defensible central estimate for a parallel-loaded fibre composite (Hashin and Shtrikman, 1963; Halpin and Kardos, 1976; Cox, 1952), so we keep it as the nominal estimate and present the bracket, with the floor inside it, as the honest position. The gap between the bounds can be narrowed only by a more favourable composite architecture—oriented or textile fibres that bring the load sharing closer to the parallel limit (Todros et al., 2015; Pott et al., 2012; Heidari et al., 2024)—or by a faster tissue response; this is the structural counterpart of §5.4; in both uncertainty dimensions the margin is thin and mesh design alone cannot guarantee it.

5.6 Limitations

Several limitations bound these conclusions. First, the model is reduced-order and lumped: it carries no spatial gradient, anisotropy, or dependence on load orientation, all of which matter at the implant scale. Second, swelling is treated as quasi-steady (Flory–Rehner), and there is no dynamic fluid phase, inflammation, or infection—processes known to alter integration. Third, the calibration is to a single material, Phasix (P4HB) (Deeken and Matthews, 2013; Martin and Williams, 2003); transferability to other resorbables such as PDO or Bio-A (Fatkhudinov et al., 2018; Heidari et al., 2024) is plausible at the level of the *levers*—rate-matching is chemistry-agnostic—but is unverified. Fourth, the Voigt central estimate with its lower-bound bracket is a bound, not a resolved property, and the true composite response lies between. Fifth, the stiffness is linearised; a finite-strain (Gent) correction (Gent, 1996) is not applied, and the single fitted value of B_{e0} carries no identifiability interval. Finally, the rupture floor $S_{\min}$ and the reference strength B_{ref} are normative choices, and the analysis uses generic rather than patient-specific loading. None of these undermines the qualitative conclusions—shared levers, matched rates, and tissue co-determination—but each sets a bound on the quantitative margin.

6 Conclusion

We presented a reduced-order coupled-ODE model that resolves the coupled chemistry, biology, and architecture of a biodegradable hernia mesh into the time-dependent strength and stiffness of the implant–tissue composite, calibrated to Phasix (P4HB) data. The model exposes a *strength valley* as the decisive risk window of the polymer-to-tissue hand-off, shows that both strength and stiffness are governed by five shared levers, and converts the qualitative principle of matching degradation to tissue integration into quantitative, parameter-level design guidance: bound the hydrolysis rate and swelling, hold the crosslink fragility low, and choose a mid-range pore size, so that degradation and integration stay rate-matched. Two honest results qualify this guidance. The safe window is *co-owned by the tissue side*: under adverse tissue kinetics no mesh design alone remains safe, which both directs attention to tissue-side adjuncts and reinterprets a class of recurrences as tissue rather than mesh failures. And the safety margin is *conditional on the composite mixing rule*: the lower bound brackets the strength valley across the rupture floor, so the margin is real but not guaranteed. The framework is chemistry-agnostic in its levers and so extends, with recalibration, to other resorbable materials; natural next steps are spatial and anisotropic mechanics, finite-strain stiffness, patient-specific loading, and prospective validation against clinical recurrence.

A All pairwise design-variable slices

The main text maps the strength valley on two representative design-variable planes ($k_{h0} \times \phi$ and $Q_0 \times \alpha_x$). Figure 10 collects all six $\binom{4}{2} = 6$ pairwise slices for completeness. The four design variables have only two qualitative structures: ϕ is the sole non-monotone lever, so the three planes containing ϕ show the interior pore optimum, while k_{h0}, Q_0, α_x are monotone, so the three planes without ϕ are smooth gradients (only the corner of high values fails). The slice safe-fractions range from 30% (planes containing k_{h0}, the dominant lever) to 88% ($\phi \times \alpha_x$); the full four-dimensional safe volume is $\approx$21% (§4.4).

References

References

Flory, P. J. & Rehner, J. Statistical mechanics of cross-linked polymer networks I. Rubberlike elasticity. *J. Chem. Phys.* **11**, 512 (1943).

Flory, P. J. & Rehner, J. Statistical mechanics of cross-linked polymer networks II. Swelling. *J. Chem. Phys.* **11**, 521 (1943).

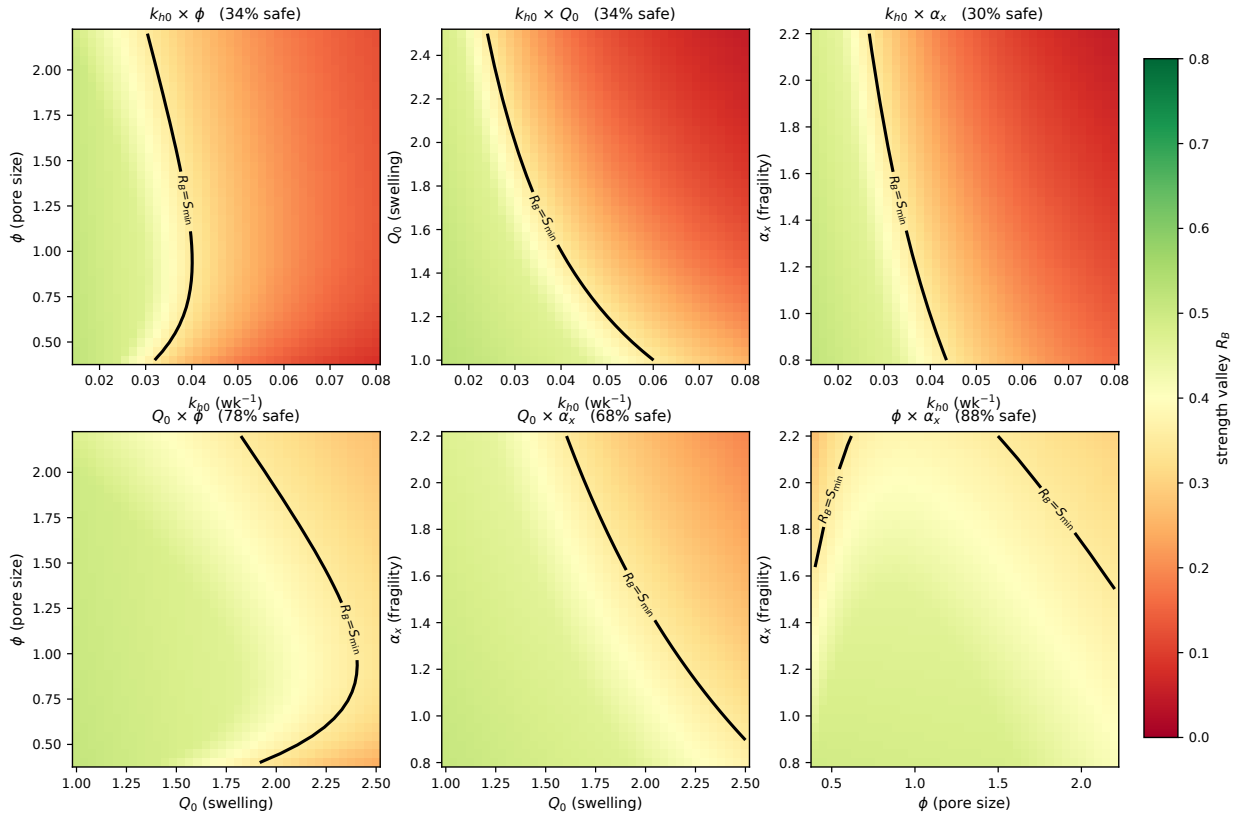

Figure 10: All six pairwise strength safe-design slices (R_B; black contour = rupture floor $S_{\min}$), the two non-axis design variables held at the calibrated baseline. (a–c) Planes containing k_{h0}, the dominant lever ($\approx$ 30–34% safe). (d–f) Planes without k_{h0} (68–88% safe). The three ϕ-planes show the interior pore optimum; the three non-ϕ planes are monotone gradients.

Peppas, N. A. & Merrill, E. W. Crosslinked poly(vinyl alcohol) hydrogels as swollen elastic networks. *J. Appl. Polym. Sci.* **21**, 1763 (1977).

Anseth, K. S., Bowman, C. N. & Brannon-Peppas, L. Mechanical properties of hydrogels and their experimental determination. *Biomaterials* **17**, 1647 (1996).

Vert, M., Li, S. M., Spenlehauer, G. & Guerin, P. Bioresorbability and biocompatibility of aliphatic polyesters. *J. Mater. Sci. Mater. Med.* **3**, 432 (1992).

Grizzi, I., Garreau, H., Li, S. & Vert, M. Hydrolytic degradation of devices based on poly(dl-lactic acid): size-dependence. *Biomaterials* **16**, 305 (1995).

Göpferich, A. Mechanisms of polymer degradation and erosion. *Biomaterials* **17**, 103 (1996).

Metters, A. T., Bowman, C. N. & Anseth, K. S. A statistical kinetic model for the bulk degradation of PLA-b-PEG-b-PLA hydrogel networks. *J. Phys. Chem. B* **104**, 7043 (2000).

Ford Versypt, A. N., Pack, D. W. & Braatz, R. D. Mathematical modeling of drug delivery from autocatalytically degradable PLGA microspheres. *J. Control. Release* **165**, 29 (2013).

Martin, D. P. & Williams, S. F. Medical applications of poly-4-hydroxybutyrate: a strong flexible absorbable biomaterial. *Biochem. Eng. J.* **16**, 97 (2003).

Lutolf, M. P. et al. Synthetic matrix-metalloproteinase-sensitive hydrogels for the conduction of tissue regeneration. *Proc. Natl. Acad. Sci. USA* **100**, 5413 (2003).

Patterson, J. & Hubbell, J. A. Enhanced proteolytic degradation of molecularly engineered PEG hydrogels. *Biomaterials* **31**, 7836 (2010).

Visse, R. & Nagase, H. Matrix metalloproteinases and tissue inhibitors of metalloproteinases. *Circ. Res.* **92**, 827 (2003).

Kagan, H. M. & Li, W. Lysyl oxidase: properties, specificity, and biological roles. *J. Cell. Biochem.* **88**, 660 (2003).

Tomasek, J. J., Gabbiani, G., Hinz, B., Chaponnier, C. & Brown, R. A. Myofibroblasts and mechano-regulation of connective tissue remodelling. *Nat. Rev. Mol. Cell Biol.* **3**, 349 (2002).

Gurtner, G. C., Werner, S., Barrandon, Y. & Longaker, M. T. Wound repair and regeneration. *Nature* **453**, 314–321 (2008).

Engler, A. J., Sen, S., Sweeney, H. L. & Discher, D. E. Matrix elasticity directs stem cell lineage specification. *Cell* **126**, 677 (2006).

Deeken, C. R. & Lake, S. P. Mechanical properties of the abdominal wall and biomaterials utilized for hernia repair. *J. Mech. Behav. Biomed. Mater.* **74**, 411 (2017).

Brown, C. N. Which mesh for hernia repair? *Ann. R. Coll. Surg. Engl.* **92**, 272 (2010).

Pott, P. P. et al. Mechanical properties of mesh materials used for hernia repair and soft tissue augmentation. *PLoS ONE* **7**, e46978 (2012).

Todros, S., Pavan, P. G., Pachera, P. et al. Synthetic surgical meshes in abdominal wall surgery: biomechanical aspects. *J. Biomed. Mater. Res. B* **103**, 890 (2015).

Bilsel, Y. & Abci, I. The search for ideal hernia repair; mesh materials and types. *Int. J. Surg.* **10**, 317 (2012).

Deeken, C. R. & Matthews, B. D. Characterization of the mechanical strength, resorption properties and histology of Phasix mesh in a porcine hernia model. *ISRN Surgery* **2013**, 238067 (2013).

Bellón, J. M. et al. Partially absorbable meshes for hernia repair offer advantages over nonabsorbable meshes. *Am. J. Surg.* **193**, 16 (2007).

Pascual, G. et al. Repair of abdominal wall defects with biodegradable laminar prostheses. *PLoS ONE* **7**, e52628 (2012).

Fatkhudinov, T. et al. Evaluation of resorbable polydioxanone and polyglycolic acid meshes in a rat model of ventral hernia repair. *J. Biomed. Mater. Res. B* **106**, 1023 (2018).

Shiroud Heidari, B., Dodda, J. M. & El-Khordagui, L. K. Emerging materials and technologies for advancing bioresorbable surgical meshes. *Acta Biomater.* **174**, 1 (2024).

Hutmacher, D. W. Scaffold design and fabrication technologies for engineering tissues. *J. Biomater. Sci. Polym. Ed.* **12**, 107 (2001).

Drury, J. L. & Mooney, D. J. Hydrogels for tissue engineering: scaffold design variables and applications. *Biomaterials* **24**, 4337 (2003).

Hollister, S. J. Porous scaffold design for tissue engineering. *Nat. Mater.* **4**, 518 (2005).

Hashin, Z. & Shtrikman, S. A variational approach to the theory of the elastic behaviour of multiphase materials. *J. Mech. Phys. Solids* **11**, 127 (1963).

Halpin, J. C. & Kardos, J. L. The Halpin–Tsai equations: a review. *Polym. Eng. Sci.* **16**, 344 (1976).

Cox, H. L. The elasticity and strength of paper and other fibrous materials. *Br. J. Appl. Phys.* **3**, 72 (1952).

Prendergast, P. J., Huiskes, R. & Søballe, K. Biophysical stimuli on cells during tissue differentiation at implant interfaces. *J. Biomech.* **30**, 539 (1997).

Lacroix, D. & Prendergast, P. J. A mechano-regulation model for tissue differentiation around non-cemented hip prostheses. *J. Biomech.* **35**, 163 (2002).

Checa, S. & Prendergast, P. J. A mechanobiological model for tissue differentiation that includes angiogenesis: a lattice-based approach. *Ann. Biomed. Eng.* **37**, 129 (2009).

Byrne, D. P., Lacroix, D. & Prendergast, P. J. Simulation of fracture healing in the tibia. *J. Orthop. Res.* **29**, 1496 (2011).

Sandino, C., Planell, J. A. & Lacroix, D. A finite element study of mechanical stimuli in scaffolds for bone tissue engineering. *J. Biomech.* **41**, 1005 (2008).

Dhote, V., Sreenivas, K., Jillavenkatesa, A. et al. Mathematical model of the role of degradation on matrix development in hydrogel scaffolds. *Biomech. Model. Mechanobiol.* **12**, 1191 (2013).

Akalp, U., Chuang, Y., Lannutti, J. & Winter, J. Tuning tissue growth with scaffold degradation in enzyme-sensitive hydrogels. *Soft Matter* **12**, 4001 (2016).

Chen, Y., Zhou, S. & Li, Q. Microstructure design of biodegradable scaffold and its effect on tissue regeneration. *Biomaterials* **32**, 3803 (2011).

Emmert, M. Y. et al. Computational modeling guides tissue-engineered heart valve design for growth and remodeling. *Sci. Transl. Med.* **10**, eaan4587 (2018).

Pan, Y., Liu, Z., Bhattacharya, K. et al. Constitutive modelling of hydrolytic degradation in hydrogels. *J. Mech. Phys. Solids* **165**, 104944 (2022).

MacKintosh, F. C., Käs, J. & Janmey, P. A. Elasticity of semiflexible biopolymer networks. *Phys. Rev. Lett.* **75**, 4425 (1995).

Storm, C., Pastore, J. J., MacKintosh, F. C., Lubensky, T. C. & Janmey, P. A. Nonlinear elasticity in biological gels. *Nature* **435**, 191 (2005).

Raub, C. B., Unruh, J., Suresh, V. et al. Image correlation spectroscopy of multiphoton images correlates with collagen mechanical properties. *Biophys. J.* **94**, 2257 (2008).

Gent, A. N. A new constitutive relation for rubber. *Rubber Chem. Technol.* **69**, 59–61 (1996).

Marino, S., Hogue, I. B., Ray, C. J. & Kirschner, D. E. A methodology for performing global uncertainty and sensitivity analysis in systems biology. *J. Theor. Biol.* **254**, 178–196 (2008).